Journal of Materials Chemistry A

ROYAL SOCIETY OF CHEMISTRY

PAPER

View Article Online
View Journal

Cite this: DOI: 10.1039/d6ta00283h

Exploiting nickel–organic-frameworks in the temperature-controlled synthesis of carbonized nickel nanoparticles for magnetic purification of acidic water

Mona Fadel, [a] A. Gallo-Córdova, [b] Pablo Álvarez-Alonso, [ac] Alberto Castro-Muñiz, [d] A. Adawy, [a] Jesús A. Blanco, [a] Montserrat Rivas, [ac] J. I. Paredes, [d] Fabián Suárez-García*[d] and Pedro Gorria *[ac]

This work explores the effect of carbonization temperature (600 °C *vs.* 1000 °C) on the microstructure, magnetic properties, and adsorption performance of nickel organic framework (NiOF)-derived nanoparticles (NPs) for the remediation of acidic water using Cr(VI) and methylene blue (MB) as a typical heavy metal and organic dye, respectively. Carbonizing NiOF at 600 °C resulted in the formation of Ni NPs with both face-centered cubic (FCC) and hexagonal-close-packed (HCP) crystal structures, with subsequent encapsulation in multilayered graphitic carbon that serves as a protective barrier against Ni NP oxidation. However, carbonization of NiOF at 1000 °C induced the formation of FCC Ni NPs exclusively, accompanied by a substantial increase in saturation magnetization. After ethanol purification, these NPs showed ferromagnetic character that allows for rapid and efficient magnetic recovery. Further purification through double water washing markedly improves adsorption kinetics, achieving equilibrium for Cr(VI) and MB within 5–12 minutes. This enhancement is attributed to greater accessibility of active sites and increased surface functional group density. Adsorption kinetics are adequately described by both pseudo-first-order and pseudo-second-order models; however, kinetic fitting alone is insufficient to elucidate the underlying mechanism. Instead, mechanistic interpretation is supported by independent evidence, including pH-dependent ζ-potential measurements, pollutant speciation, and textural and microstructural characterization. These results indicate that, at pH 3, Cr(VI) uptake is primarily governed by electrostatic attraction, whereas MB adsorption is dominated by π–π stacking and dispersion interactions on more graphitic surfaces. These findings underscore the carbonization temperature as a critical parameter for tailoring the structural, magnetic, and adsorption properties of NiOF-derived NPs, enabling the design of high-performance, magnetically recoverable adsorbents for water purification.

Received 11th January 2026
Accepted 23rd March 2026

DOI: 10.1039/d6ta00283h

rsc.li/materials-a

1 Introduction

There is an urgent need to prioritize research on innovative materials to address, mitigate, and prevent the detrimental impact caused by industrial and anthropogenic activities on the environment, particularly soil, water, and air. Among the various strategies under investigation, engineered nanomaterials have attracted considerable attention for environmental diagnosis and remediation owing to their high surface area, tunable physicochemical properties, and enhanced reactivity.[1–6] In particular, water contamination by synthetic dyes and heavy metals remains a critical global challenge, as these pollutants are chemically stable, persistent, and difficult to remove using conventional treatment technologies.[7] Two pollutants of major global environmental concern are hexavalent chromium (Cr(VI))[8] and methylene blue (MB).[9] Cr(VI) is highly toxic, carcinogenic, and non-biodegradable, exhibiting long-term persistence in natural waters and posing severe risks to human health and ecosystems.[10,11] Industrial effluents and wastewater are the primary sources of Cr(VI) contamination, particularly from sectors such as electroplating, metal finishing, and leather tanning.[12] The latter sectors also generate large volumes of dye-containing wastewater. Among them, MB is a synthetic cationic dye extensively used in the textile, paper, and pharmaceutical industries. Owing to its high chemical stability and resistance to biodegradation, MB accumulates in aquatic environments, where it reduces light

[a]*Departamento de Física, Universidad de Oviedo, C/Calvo Sotelo 18, 33007, Oviedo, Spain. E-mail: pgorria@uniovi.es*

[b]*Institute of Material Science of Madrid, ICMM/CSIC, C/Sor Juana Inés de la Cruz 3, 28049 Madrid, Spain*

[c]*IUTA, Universidad de Oviedo, 33203 Gijón, Spain*

[d]*Instituto de Ciencia y Tecnología del Carbono, INCAR-CSIC, C/Francisco Pintado Fe 26, 33011 Oviedo, Spain. E-mail: fabian.suarez@csic.es*

penetration, disrupts photosynthetic processes, and exerts toxic effects on aquatic organisms and humans.[13,14]

Beyond the presence of toxic metals and synthetic dyes, industrial wastewater is often characterized by highly acidic conditions, which further complicate remediation strategies. Acidic effluents represent an additional and critical environmental challenge, particularly in industries such as the previously mentioned leather tanning sector, which is not only a major contributor to Cr(VI) and MB contamination but also a significant source of low-pH discharges.[15,16] In addition, within tanneries, the primary source of acidic wastewater arises from the pickling stage, where strong acids (typically sulfuric or formic acid) are introduced to lower the pH of hides to approximately 2.5–3.5. This process stabilizes collagen fibers and facilitates the subsequent uptake of chromium-based tanning agents. After pickling, the process water—containing residual acids and dissolved contaminants—is discharged, significantly contributing to environmental acidification.[17] Acidic effluents are also generated in other industrial processes, such as underground coal gasification, an emerging energy extraction technology that produces wastewater enriched with toxic and persistent compounds. In this case, the low pH arises mainly from the formation of acidic gases (*e.g.*, sulfur and carbon oxides) and the leaching of acidic species from coal seams and surrounding rock formations.[18,19] Together, these examples highlight the urgent need for water treatment technologies that can operate efficiently under strongly acidic conditions.

To overcome the persistent challenge of treating acidic industrial wastewater, we investigate adsorption under strongly acidic conditions (pH 3), a level representative of typical tannery effluents and directly relevant to real-world applications. In this context, magnetic NPs coated with carbon-based materials emerge as a promising, sustainable, and cost-effective platform for water purification. Their intrinsic magnetic response enables rapid and efficient post-treatment recovery, minimizing secondary pollution, while the carbon shell enhances chemical stability, surface functionality, and resistance to harsh environments and can additionally impart catalytic or photocatalytic activity.[20,21] Achieving high remediation performance requires a delicate balance of key material properties, including nanoscale particle dimensions for colloidal stability and high surface-to-volume ratios, accessible surface functional groups for effective adsorption, and sufficient magnetic moments to ensure fast and reliable magnetic separation.

While our group has previously reported Ni@C NPs and NiOF-derived materials for catalytic and magnetic hyperthermia applications,[22–24] the present study introduces several distinct advances. In particular, this is the first study from our group to integrate magnetic recoverability with rapid adsorption kinetics for pollutant removal. Herein, Ni@C nanomaterials are evaluated as magnetically recoverable adsorbents for the elimination of representative inorganic and organic contaminants from polluted water, using Cr(VI) as a model heavy metal and MB as a model organic dye. Given that the magnetic response and microstructure of Ni@C hybrids are highly sensitive to carbonization temperature,[22,23] two carbonization conditions (600 and 1000 °C) were deliberately selected to access distinct magnetic regimes, namely single-domain and multidomain behaviour, respectively. This strategy enables a systematic investigation of how temperature-induced phase evolution, carbon shell structure, and magnetic properties collectively govern adsorption kinetics and removal efficiency under acidic conditions.

To ensure a chemically accessible and well-defined surface, the as-prepared materials were subjected to rigorous purification to remove amorphous carbon and residual impurities. This step is essential not only to prevent filtration artifacts during adsorption experiments but also to preserve strong magnetic responsiveness for rapid post-treatment recovery. By directly comparing the performance of Ni@C NPs carbonized at different temperatures, this study aims to elucidate whether increasing the carbonization temperature can enhance contaminant removal while maintaining efficient magnetic separability, thereby establishing clear structure–property–function relationships for the rational design of advanced water purification materials.

2 Experimental methods

2.1 Synthesis and sample preparation

The synthesis methodology, previously reported by Martín-Jimeno *et al.*,[24] consists of two steps: (1) chemical synthesis of a Ni-based metal–organic framework (NiOF) and (2) NiOF carbonization at 600 and 1000 °C under an inert atmosphere. Nickel acetate tetrahydrate ($Ni(OAc)_2 \cdot 4H_2O$, 99%), 2-methylimidazole ($C_4H_6N_2$, 2-mIm, 99%), methylene blue, and potassium dichromate ($K_2Cr_2O_7$ > 99%) were purchased from Sigma-Aldrich (Merck) and were used without any further purification. Further details about the synthesis procedure are given in Section S1 of the SI.

Some portions of the carbonized samples, labeled S600 and S1000 hereafter, were washed with ethanol. Magnetic harvesting was used to remove non-magnetic residues. After washing, the samples were air-dried at room temperature (RT) for 24 hours and then subsequently dried at 30 °C for 2 hours. The washed samples were labeled S600-2W, S600-3W, S1000-2W, and S1000-3W, where the number before "W" denotes the number of washing cycles performed.

2.2 Physical–chemical characterization

Room temperature X-ray powder diffraction (XRD) patterns were recorded using a Philips X'Pert PRO MPD diffractometer with Cu $K_{\alpha 1}$ monochromatic radiation ($\lambda = 1.5406$ Å) to determine the crystalline structure and microstructure of the samples. Standard LaB_6 was used for instrument resolution, and full profile analysis of the diffraction patterns was carried out using the FullProf suite package based on the Rietveld method.[25] The mass percentage of Ni in the samples was obtained from thermogravimetric analysis (TGA) using an SDT Q600 device (TA Instruments) under an air flow with a heating program of 10 °C min^{-1} up to 950 °C and keeping this temperature constant for 30 min. Several factors may contribute to the uncertainty in the Ni mass determination, such as incomplete oxidation of the sample, overlapping thermal events

(*e.g.*, carbon combustion and Ni oxidation), and the presence of residual carbon at high temperatures. However, gasification in air at temperatures above 900 °C completely removes the carbonaceous residue,[26] while the metallic Ni is fully converted to NiO,[27] something that occurs entirely in the case of nanoparticles. Therefore, the mass of Ni in the starting material can be determined with high accuracy using this method. High-resolution transmission electron microscopy (HRTEM) images were obtained using a JEOL JEM-2100F microscope (200 kV). A small amount of powder was dispersed in ethanol, and several drops of the solution were deposited onto lacey-carbon coated copper grids. NP-size histograms were constructed from randomly selected NPs (more than 400) in several TEM micrographs using ImageJ[28] software and fitted using a log-normal function to obtain the characteristic parameters of the NP-size distribution in each sample.

Hysteresis loops $M(H)$ were measured at RT using a Quantum Design PPMS-14T equipped with a vibrating sample magnetometer (VSM), under an applied magnetic field within the ±20 kOe (±1.6 MA m^{-1}) range. We analyzed the magnetic dragging capacity and velocity of the NPs in deionized water (3 mg mL^{-1}). The dispersion was shaken in a polystyrene optical cuvette, and the turbid solution was immediately excited with a mW HeNe-gas laser (632.8 nm). Transmitted light was measured with a photometer linked to a multimeter (Meterman). A magnet (with an approximate gradient value of $\nabla B = 22$ T m^{-1}) was placed beneath the cuvette to separate the magnetic Ni@C NPs, and transmitted light was measured over time. All measurements were carried out at room temperature.

N_2 adsorption–desorption isotherms were measured at $T =$ 77 K (−196 °C) using a volumetric apparatus (ASAP 2010, Micromeritics). Prior to analysis, the samples were degassed at 150 °C overnight. From the adsorption branch of the isotherms, the apparent surface area (S_{BET}) was determined using the Brunauer–Emmett–Teller (BET) method[29] within the relative pressure range of 0.01 to 0.25. The micropore volume (V_{DR}, N_2) was calculated using the Dubinin–Radushkevich (DR) equation in the relative pressure range of 0.001 to 0.15. The total pore volume (V_T) was estimated based on the volume of liquid nitrogen adsorbed at a relative pressure of 0.975.[30] We measured the ζ-potential of the NPs by Dynamic Light Scattering (DLS) using a Litesizer DLS 700 (Anton Paar) to assess the surface charge characteristics of the Ni@C NPs in aqueous media at pH 3.

2.3 Pollutant adsorption

The magnetic nanoadsorbents were tested for Cr(VI) and MB removal, whose concentrations were assessed using a Varian Cary 50 Bio UV-visible spectrophotometer. The samples were analyzed at wavelengths $\lambda = 350$ nm and 665 nm, respectively. For this purpose, absorbance *versus* concentration calibration curves were measured using standard dilutions, considering first stock solutions of 500 mg L^{-1} of Cr(VI) and MB. For the calibration curves, the Cr(VI) concentrations varied between 10 and 100 mg L^{-1}, while the MB concentrations varied between 1 and 5 mg L^{-1}, yielding linear correlation factors R^2 of 0.995 and 0.996, respectively.

We used 15 mL plastic conical vials for the adsorption experiments, each containing 10 mL of MB and Cr(VI) solutions and 10 mg of the Ni@C sample, which were agitated with a mechanical shaker (GFL 3015) at 400 rpm. After the incubation contact time, Ni@C was swiftly collected within 5 minutes using magnetic harvesting with a 60 mm × 30 mm magnet that generates a surface field strength of 0.4 kA m^{-1}, and the remaining pollutant concentration in the supernatant was measured by spectrophotometry.

3 Results and discussion

3.1 Structural and morphological characterization

The XRD patterns for the S600-2W and S1000-2W washed samples are shown in Fig. 1, while the diffractograms for the S1000 and S600 samples are depicted in Fig. S1 of the SI. For the

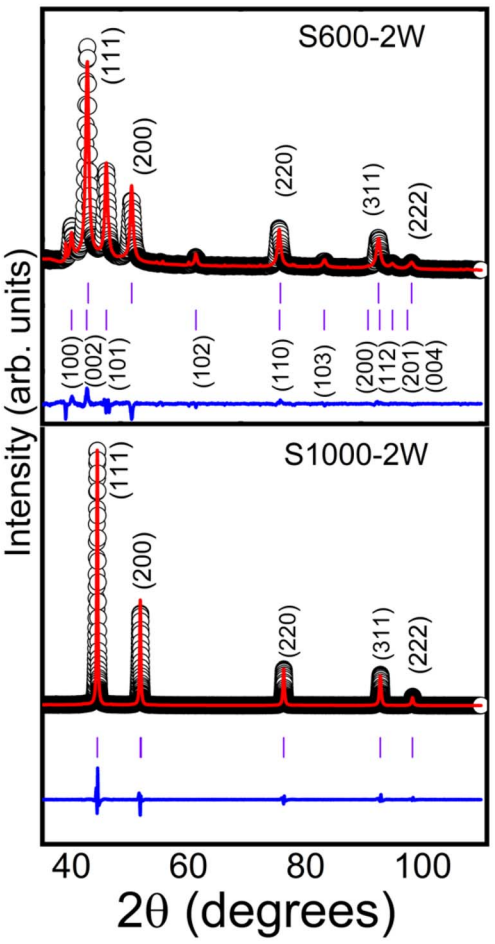

Fig. 1 Room temperature X-ray powder diffraction patterns of S600-2W and S1000-2W samples. Black open circles and red solid lines represent the experimental data and the corresponding fit, respectively. A solid blue line at the bottom is the difference between the experimental data and the theoretical model. The first series of vertical bars correspond to the positions of the Bragg reflections associated with the crystal structure of FCC-Ni, and the second one with that of HCP-Ni.

Table 1 Results from structural and morphological characterization: X_{Ni} represents the mass fraction of Ni in the samples, as determined by TGA measurements. $X_{FCC\text{-}Ni}$ and $X_{HCP\text{-}Ni}$ correspond to the mass percentages of the FCC and HCP crystalline phases, respectively. D_{XRD} denotes the crystallite size estimated from XRD data. The ζ-potential and the effective saturation magnetization (in the CGS system, the magnetization expressed in emu per g-Ni has the same numerical value as in A per m^2 per kg-Ni in the SI system)

Sample	X_{Ni} (wt%)	$X_{FCC\text{-}Ni}$ (%)	$X_{HCP\text{-}Ni}$ (%)	D_{XRD} (nm)	ζ potential (mV)	M_s (emu per g-Ni)
S600	46.7	57(2)	42(2)	11(1)	24.5	32(2)
S1000	50.7	100	—	64(1)	9.7	50(3)
S600-2W	43.2	60(2)	40(2)	13(1)	19.6	31(2)
S1000-2W	48.2	100	—	64(1)	21.1	50(3)

S600-2W sample, we can observe Bragg reflections associated with the face-centered cubic FCC ($Fm\bar{3}m$) and hexagonal close-packed HCP ($P6_3/mmc$) crystalline structures of Ni, with cell parameters $a = 3.525$ Å for the FCC structure and $a = 2.490$ Å and $c = 4.089$ Å for the HCP structure, in agreement with previously reported values.[31,32] In contrast, the XRD pattern for

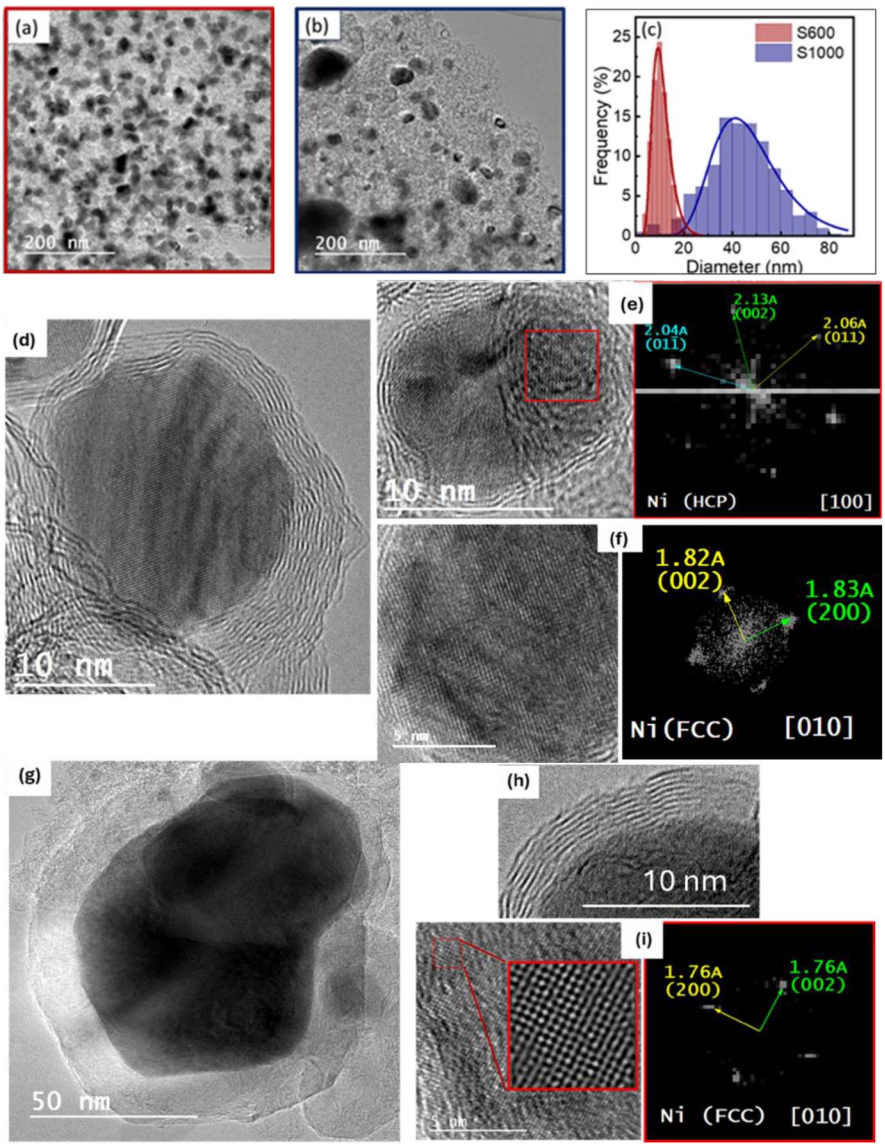

Fig. 2 Representative TEM images illustrating Ni nanoparticles embedded in the carbon matrix for (a) S600 and (b) S1000. (c) Particle size distribution histograms for both samples. (d) HRTEM image of an individual crystalline Ni NP (S600) encapsulated in graphite multilayers. (e) Left panel: HRTEM image of a carbon multilayered encapsulated NP and right panel: Fast Fourier Transform (FFT)-based crystallographic analysis of the red-squared area. (f) Left panel: HRTEM image of a NP and right panel: FFT analysis of the whole image. (g) Representative crystalline NP of the S1000 sample. (h) A magnified view of the typical turbostratic graphite coating of S1000 NPs. (i) Left panel: HRTEM image of a NP, the inset is the autocorrelation function of the small red-squared area, right panel: FFT analysis of the red-squared area.

S1000-2W exclusively display Bragg reflections corresponding to the FCC-Ni phase. A similar behaviour is observed for unwashed samples, as illustrated in Fig. S1. It is worth noting that the width of the diffraction peaks for S600-2W is similar to that of S1000-2W NPs (Fig. S2 of the SI), indicating a similar crystallite size of both specimens.

The structural parameters obtained from Rietveld refinement of the XRD patterns were combined with the Scherrer peak-broadening method.[33] The results are summarized in Table 1, revealing average crystallite sizes of 13 nm and 64 nm for S600-2W and S1000-2W NPs, respectively.

The TEM images shown in Fig. 2(a) and (b) reveal quasi-spherical Ni NPs intricately embedded within the carbonaceous matrix. By analyzing these images, we estimated the NP mean size from the fit to a log-normal distribution of the resulting histograms [Fig. 2(c)], giving values of 11 nm for S600 and 50 nm for S1000, confirming an abrupt NP growth with increasing carbonization temperature, as also inferred from XRD data. HRTEM images show that the Ni NPs are coated with around seven to ten turbostratic carbon layers in the S600 [Fig. 2(d)] and S1000 samples [Fig. 2(h)]. These graphitic shells effectively protect the NP surface from oxidation, as reported in similar hybrid materials synthesized with sucrose.[34,35] In the absence of this protective layer, oxidation would typically lead to the formation of an antiferromagnetic NiO shell,[36] a phase not detected by XRD in our samples. The formation of this coating is attributed to the transformation of NiOF into a Ni metal–carbon composite during the carbonization process.[22] The organic precursor (*i.e.*, 2-mIm) is thermally decomposed, resulting in the formation of a carbonaceous material that surrounds the Ni NPs.[22,36] In addition, the analysis of HRTEM images confirms that S600 exhibits both HCP and FCC Ni crystal structures [Fig. 2(e) and (f)], whereas only the FCC phase is observed in S1000 [Fig. 2(k)]. Furthermore, the rhombohedral ($R\bar{3}c$) Ni_3C phase has been detected in the S600 sample (not shown), but not in S1000. The absence of this rhombohedral phase in the XRD patterns is attributed to its crystallite size being below the detection limit of the technique.[22,23]

Based on the TGA results presented in Table 1 and Fig. S3, we can infer some of the effects of removing the non-magnetic components (excluding the C coating of the Ni particles, which is considered an intrinsic part of the Ni NPs). Upon washing, the Ni content slightly decreases, a counterintuitive result, considering that the process primarily removes loosely bound non-magnetic carbon. A possible explanation is that extremely small Ni particles with weak magnetism are also eliminated during washing. This effect is particularly evident in the case of S600, which contains smaller Ni NPs (see Fig. 2) and a non-magnetic HCP-Ni fraction. This interpretation is supported by the slight increase in the estimated crystallite size of S600 after washing.

3.2 Magnetic properties

Fig. 3 represents the magnetization curves, measured under a DC magnetic field ranging from −20 to 20 kOe (from −1.6 to 1.6 MA m^{-1}), for both S600-2W and S1000-2W samples. The

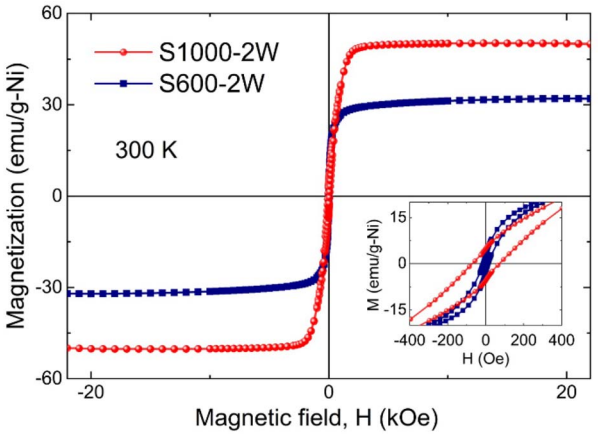

Fig. 3 Magnetization *versus* applied magnetic field curves measured at $T = 300$ K. The inset shows the low-field region of the hysteresis loops. In SI units, the magnetization values are the same as in A m^2 per kg-Ni, whereas the magnetic field (A m^{-1}) is obtained from the CGS values by multiplying by a factor of $10^3/(4\pi)$.

magnetization was normalized to the Ni content, based on the fraction of Ni in the samples obtained by TGA (see Table 1).

The inset shows a weak hysteretic behaviour for the S600-2W sample, with a coercive field of 13 Oe (1.04 kA m^{-1}) and a magnetic remanence of 2.6 emu per g-Ni (or A m^2 kg^{-1}). In contrast, the S1000 sample exhibits a higher coercive field of 83 Oe (6.61 kA m^{-1}) and a remanence of 4.9 emu per g-Ni. We estimated the saturation magnetization (M_s) using the approach-to-saturation law,[37] $M = M_s\left(1 - \frac{a}{H} - \frac{b}{H^2}\right) + \chi H$,

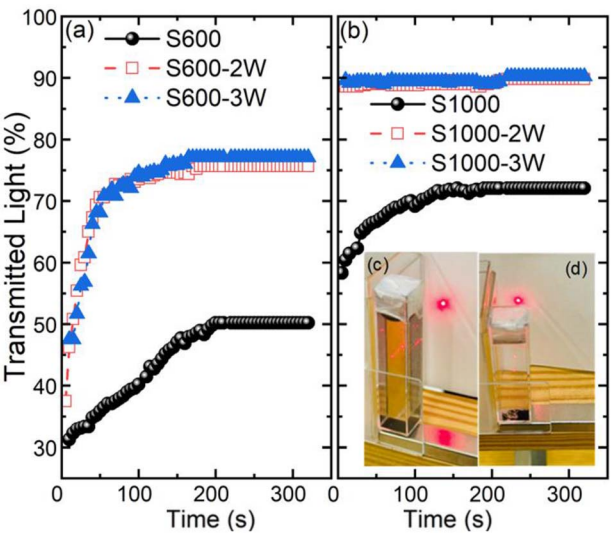

Fig. 4 Transmitted light (%) over time for (a) S600 and (b) S1000. The solid dark circles represent the original samples (S600 and S1000), the red dashed rectangles correspond to the samples washed twice (S600-2W and S1000-2W), and the blue dotted triangles represent the samples washed three times (S600-3W and S1000-3W) in water suspension. The insets show photographs of the separated solutions for (c) S600-2W and (d) S1000-2W.

where a, b, and χ are fitting constants. For S1000 NPs, we find a M_s value of 50.3 emu per g-Ni, very close to the reported value for bulk FCC-Ni at RT (55.1 emu per g-Ni).[38] For S600 NPs, M_s = 31.8 emu per g-Ni, which is smaller due to the presence of paramagnetic HCP-Ni and Ni_3C phases (≈40 wt%).[22] Indeed, the HCP phase is expected to reduce exchange interactions, reducing saturation magnetization.[39,40] These findings corroborate the results from the structural characterization, with the increase in the FCC-Ni phase at higher carbonization temperatures.

3.3 Magnetic separation

Our aim is to achieve a solution that relies solely on magnetic removal, eliminating the need for any filtration process during the adsorption experiments. This approach ensures that no residue remains in the solution and that all the adsorbent is recovered, allowing it to be reused. Therefore, it is essential to evaluate the magnetic drag capacity of the nanoadsorbents. In Fig. 4(a) and (b) we show the magnetic separation curves, derived from the light transmission measurements through the supernatant [see Fig. 4(c) and (d)].

The results reveal a remarkably fast process for all samples. Measurements were taken for 5 minutes to ensure a large removal percentage. Among the studied samples, S600 has the weakest performance, with 50% of the material removed from the fluid, which is easily explained by the smaller particle size and the large non-ferromagnetic portion of Ni NPs. Magnetic separation becomes significantly faster after two ethanol washing cycles (S600-2W and S1000-2W), reaching 80% of transmitted light in 3 minutes with S600-2W and 90% of transmitted light almost instantaneously (less than 5 seconds, our time measurement interval) with S1000-2W. Additional purification steps do not result in a significant improvement. Given that two washing cycles substantially improve magnetic separation efficiency, the results presented hereafter emphasize the washed samples S600-2W and S1000-2W. Data for the unwashed references (S600 and S1000) are provided for comparative purposes.

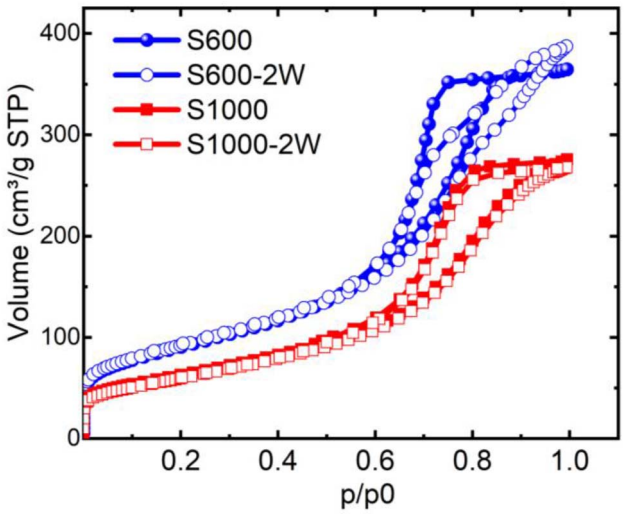

Fig. 5 N_2 adsorption–desorption isotherms under standard temperature and pressure conditions for samples S600, S600-2W, S1000, and S1000-2W.

Table 2 Porous textural parameters (superficial area S_{BET}, the total volume V_T, and mesoporous volume V_{DR}) derived from N_2 adsorption measurements at −196 °C for the S600 and S1000 samples, and their washed counterparts

Sample	V_T ($cm^3\ g^{-1}$)	V_{DR} ($cm^3\ g^{-1}$)	S_{BET} ($cm^2\ g^{-1}$)
S600	0.56	0.12	321
S600-2W	0.58	0.12	328
S1000	0.42	0.09	222
S1000-2W	0.41	0.08	213

3.4 Porous framework characterization

The N_2 adsorption–desorption isotherms are shown in Fig. 5, with the corresponding porous textural parameters summarized in Table 2.

All Ni@C samples displayed type IV isotherms, which are characteristic of mesoporous materials. The surface area and pore volume barely change after washing, although the shape of the two isotherms at relative pressures greater than 0.7 is the same for both 600 °C samples. This range corresponds to adsorption in large mesopores. As shown in Table 2, high carbonization temperature results in a decrease in porosity, evidenced by a decrease in the surface area from over 320 to approximately 210 $cm^2\ g^{-1}$, along with corresponding diminution in both total and micropore volumes. This trend is attributed to enhanced graphitization at elevated temperatures, which promotes the reorganization of disordered carbon into more compact and ordered graphite-like microstructures. Using thermal treatments at higher temperatures, carbon defects diminish, while the stacking and lateral growth of graphitic crystallites increase, leading to a denser, less porous, and more crystalline material.[41]

3.5 Chromium(VI) and methylene blue adsorption experiments

3.5.1 Adsorption kinetics. We performed time-dependent measurements of the adsorption concentration $C(t)$ at pH = 3 using initial concentrations of C_i = 100 ppm and C_i = 80 ppm of MB and Cr(VI), respectively. Then, we calculated the adsorption capacity as $q(t) = \frac{V}{m}[C_i - C(t)]$. The insets in Fig. 6 display the experimental data together with two non-linear fits. The solid line represents the pseudo-first-order (PFO) kinetic model, in which $q(t)$ decreases exponentially with time,

$$q(t) = q_e[1 - \exp(-k_1 t)] \quad (1)$$

where q_e is the equilibrium adsorption capacity and k_1 represents the adsorption rate. This model assumes that the rate of adsorption is proportional to the number of available

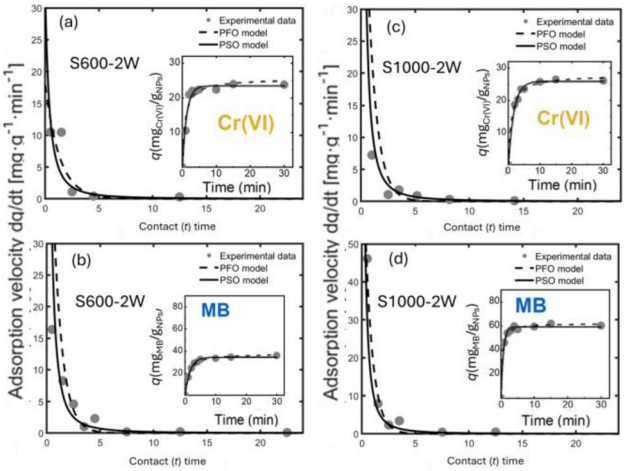

Fig. 6 Time-evolution of the adsorption velocity related to the samples S600-2W and S1000-2W for Cr(VI) and MB. The insets represent the PFO model fit (solid line) and PSO model fit (dashed line), see the text for details.

adsorption sites. The dashed line is the fitted curve following the pseudo-second-order (PSO) model:

$$q(t) = \frac{q_e^2 k_2 t}{1 + q_e k_2 t} \quad (2)$$

where k_2 is the PSO rate constant, which reflects the chemisorption rate. Additionally, we fitted the data to the intraparticle diffusion model (not shown), which describes the adsorption kinetics by evaluating the rate at which adsorbate molecules migrate from the solution into the pores of the adsorbent, using the following expression:[42]

$$q(t) = k_{int} \times t^{1/2} + C \quad (3)$$

where k_{int} represents the intraparticle diffusion rate constant (*i.e.*, the rate of diffusion of the adsorbate into the pores of the adsorbent). The main graphs in Fig. 6 depict the adsorption rate represented by the first time derivative $\dot{q}$. These graphs highlight two relevant characteristics: (i) a rapid initial adsorption stage, with rates in the range of 30–50 mg g^{-1} min^{-1}; and (ii) equilibrium is reached in approximately 8 minutes. The adsorption parameters obtained from the non-linear fits to these models are gathered in Table 3. The experimental data for MB dye and Cr(VI) adsorption on Ni@C were well described by both the PFO and PSO kinetic models, as evidenced by high correlation coefficients ($R^2 \geq 0.99$). However, the intraparticle diffusion model did not adequately fit the data, suggesting that pore diffusion was not the rate-limiting step. Based on structural and microstructural analysis of Ni@C, as well as the nature of the contaminant [Cr(VI) and MB], we propose that physical adsorption dominates.

As shown in Fig. S4, the samples exhibit a ζ-potential greater than 0 for pH ≤ 6, indicating that the surface is positively charged at acidic pH, due to protonation of surface groups. Under acidic conditions, Cr(VI) mainly exists as $HCrO_4^-$ and $Cr_2O_7^{2-}$ ions. When the pH is low, around 3, approximately 89% of Cr(VI) is present as $HCrO_4^-$ and 11% as $Cr_2O_7^{2-}$. Under the conditions used here (pH = 3), the positively charged surface of the Ni@C adsorbent electrostatically attracts these negatively charged Cr(VI) species, enhancing adsorption. The strong electrostatic interaction between the NPs and Cr(VI) fitted well with the PFO kinetic model (Table 1). However, intraparticle diffusion plays a minor role, likely due to the pore size distribution of the adsorbents. As observed in the isotherms (Fig. 5), these materials exhibit a significant presence of mesopores, particularly wide mesopores, which facilitate contaminant diffusion into the porous structure.

Additionally, the nanometric thickness of the carbon layers (Fig. 2) results in short diffusion paths to the adsorption sites, further accelerating the process. Therefore, it can be concluded that the morphology and porosity of these materials are highly favorable for the rapid Cr(VI) adsorption.

MB dye is a compound that dissociates in aqueous solutions, undergoing cationic hydrolysis in subsequent steps. The adsorption of MB molecules occurs *via* two possible mechanisms: (i) physical adsorption, involving interactions between the aromatic components of the dye and the surface of the carbon material, and (ii) electrostatic attraction of the MB cation to unprotonated surface groups of the adsorbent. The second pathway is only possible at a pH below the point of zero charge (PZC) of the carbon surface. Since the equilibrium pH of the MB solutions ranges from 3.20 to 3.81, which is lower than the PZC, the surface groups on the carbon sorbents are fully protonated. Consequently, electrostatic attraction is unlikely (in fact, adsorption *via* this pathway would be hindered due to electrostatic repulsion), suggesting that MB adsorption solely occurs *via* interactions between the electron-dislocated Lewis sites of the basal carbon planes and the aromatic dye molecules. This process is driven by physical forces such as London dispersion forces and π–π interactions.[43,44] This aligns with the

Table 3 Kinetic parameters obtained from pseudo-first-order and pseudo-second-order model fitting for samples S600-2W and S1000-2W. The estimated errors (in parentheses) are derived from the least-squares fit

		Pseudo-first order fit			Pseudo-second order fit		
Sample	Pollutant	q_e (mg g^{-1})	k_1 (min^{-1})	R^2	q_e (mg g^{-1})	k_2 (g mg^{-1} min^{-1})	R^2
S600-2W	MB	34(1)	0.60(3)	0.994	38(1)	0.020(3)	0.991
S1000-2W	MB	59(1)	1.4(1)	0.992	62(1)	0.050(6)	0.990
S600-2W	Cr(VI)	23(1)	0.8(1)	0.993	25(2)	0.06(4)	0.984
S1000-2W	Cr(VI)	21(1)	0.5(1)	0.990	23(1)	0.034(8)	0.998

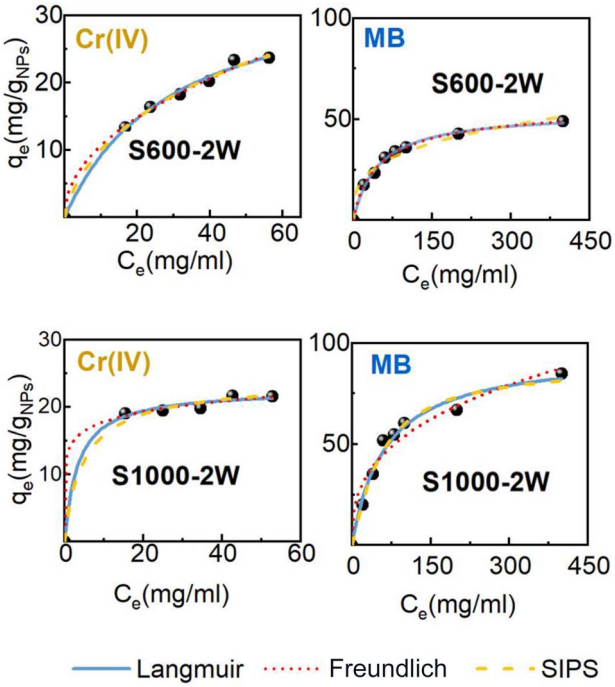

Fig. 7 Non-linear fitting of the equilibrium adsorption capacity *versus* equilibrium concentration using different isotherm models for S600-2W and S1000-2W samples with Cr(VI) and MB.

observed kinetic behaviour, where the PFO and PSO models provided the best fit. Moreover, for the same reasons described for Cr(VI), the adsorption of MB is not governed by intraparticle diffusion.

3.5.2 Adsorption isotherms. The adsorption isotherms, represented in Fig. 7, illustrate the equilibrium adsorption capacity of both MB and Cr(VI) as a function of the equilibrium concentration (C_e, the concentration of the adsorbate that remains in the solution once the adsorption process has reached equilibrium) under Standard Temperature and Pressure (STP) conditions and at pH 3, for the S600-2W and S1000-2W samples. We fitted the experimental data collected at various pollutant concentrations to the Langmuir isotherm model:

$$q_e = \frac{q_{max} \times K_L \times C_e}{1 + K_L \times C_e} \quad (4)$$

Freundlich isotherm model:

$$q_e = K_F \times C_e^{1/n_F} \quad (5)$$

and Sips isotherm model:

$$q_e = \frac{q_{max} \times K_S \times C_e^{n_S}}{1 + K_S \times C_e^{n_S}} \quad (6)$$

where K_L, the Langmuir constant, reflects the binding strength between the adsorbate and the adsorbent; K_F, the Freundlich constant, indicates the adsorption capacity according to the Freundlich model; K_S, the Sips equilibrium constant, combines features of both the Langmuir and Freundlich models to describe adsorption affinity in heterogeneous systems; n_F, the Freundlich exponent, and n_S, the Sips exponent, quantify the degree of surface heterogeneity, with lower values indicating greater heterogeneity; and q_{max} denotes the maximum adsorption capacity. Each model provides valuable insights into the adsorption process and maximum adsorption capacity.[45–47]

The values of the K_L and K_S affinity parameters (see Table 4) indicate a stronger affinity of the nanoadsorbents for Cr(VI), especially in the case of S1000-2W. This suggests robust binding interactions, likely driven by favorable electrostatic attraction between the negatively charged Cr(VI) species and the positively charged Ni@C surface at pH 3. Conversely, the lower affinity for MB is attributed to the electrostatic repulsion between it and the carbon surface at the value of pH used in these experiments. It is known that the adsorption capacity of MB by carbon materials generally increases with pH, because the charge of carbon surface becomes more negative.[48,49]

For Cr(VI) at pH 3, Sips exponents near unity ($n_S \approx 1.0$) render the model effectively Langmuir-like, consistent with a quasi-uniform site energy distribution under electrostatically favorable conditions ($\zeta > 0$; Fig. S4; $HCrO_4^-$, $Cr_2O_7^{2-}$ speciation). In contrast, MB shows $n_S \approx 0.9$–1.2, indicating moderate heterogeneity with finite saturation and hence Sips is preferred over Freundlich at high C_e. The higher maximum adsorption capacity of S600-2W for Cr(VI) compared to S1000-2W results from two key factors: (i) its greater micropore volume, which provides more adsorption sites, and (ii) its stronger electrostatic attraction, as evidenced by its significantly higher ζ-potential. However, this trend is reversed for MB adsorption, where the S1000-2W sample shows the highest q_{max} values, despite its lower S_{BET}, as confirmed by both the Langmuir and Sips models.

The superior adsorption of MB on S1000-2W can be attributed to its lower surface heterogeneity and enhanced graphitic character. With a ζ-potential of +8.2 mV (*vs.* +19.6 mV for S600-

Table 4 Calculated Langmuir, Freundlich, and Sips parameters for samples S600-2W and S1000-2W. The estimated errors (in parentheses) are derived from the least-squares fit

		Langmuir			Freundlich			Sips			
Sample	Pollutant	K_L (L mg^{-1})	q_{max} (mg g^{-1})	R^2	K_F (mg g^{-1})(mg L^{-1})^{n_F}	n_F	R^2	K_S (L mg^{-1})^{n_S}	q_{max} (mg g^{-1})	n_S	R^2
S600-2W	MB	0.021(5)	54(4)	0.995	8(1)	3.3(3)	0.972	0.018(5)	57(4)	0.9(1)	0.996
S1000-2W	MB	0.016(5)	95(5)	0.980	11(2)	2.8(4)	0.942	0.018(5)	90(9)	1.2(3)	0.978
S600-2W	Cr(VI)	0.03(1)	36 (6)	0.995	3.6(3)	2.0(4)	0.991	0.03(5)	39(8)	1.0(1)	0.995
S1000-2W	Cr(VI)	0.18(5)	29(4)	0.984	12(1)	5.0(6)	0.995	0.20(2)	30(5)	0.9(1)	0.982

2W at pH 3), S1000-2W exhibits a weaker positive surface charge, reducing electrostatic repulsion of cationic MB. More critically, the fact that we have a 100% FCC phase (*vs.* 60% in S600-2W) and larger NP size indicates a more uniform, graphitized surface[41] with fewer dispersed functional groups. This homogeneity minimizes steric and electronic disruptions, facilitating stronger π–π interactions between MB's aromatic rings and the carbon's basal planes. In contrast, the higher surface charge of sample S600-2W and mixed FCC/HCP phases introduce heterogeneity that hinders these interactions, despite its microporous advantage for Cr(VI) adsorption. Thus, the structural uniformity of S1000-2W optimizes π–π stacking, explaining its higher MB uptake.

While washing reduces the Ni content by approximately 15–20%, the magnetic performance remains largely unaffected; the samples retain sufficient saturation magnetization ($M_s \approx 50$ emu per g-Ni) to enable rapid magnetic separation. In contrast, adsorption capacity depends more critically on surface accessibility and the functional groups introduced during washing—factors that compensate for the minor loss in Ni content. Consequently, the net performance represents a favorable trade-off where the gains from surface activation exceed the modest reduction in the magnetic material. In Table S1, the maximum adsorption capacities of our Ni@C composites (S600-2W and S1000-2W) are compared with a selection of reported magnetic and non-magnetic carbon-based adsorbents for the pollutants investigated in this work, MB and Cr(VI), under comparable pH conditions.[41,42,50–55] Beyond their competitive performance in terms of maximum adsorption capacity and surface area, our materials demonstrate an additional key advantage: they reach saturation significantly faster than many systems reported in the literature, completing the adsorption process in just a few minutes. This rapid kinetics, combined with magnetic separability, makes the developed Ni@C hybrids especially attractive for practical water purification applications. Altogether, they offer an efficient, recyclable, and cost-effective platform for environmental remediation technologies.

4 Summary and conclusions

Our investigation demonstrates the significant influence of carbonization temperature and post-treatment washing on tuning the structural, magnetic, and adsorption properties of NiOF-derived Ni@C NPs. The sample carbonized at 600 °C (S600) exhibits a mixture of FCC and HCP Ni crystalline phases, whereas increasing the carbonization temperature to 1000 °C (S1000) results in highly crystalline FCC-Ni with enhanced saturation magnetization. Magnetic separation experiments confirm the practical applicability of these materials. Among the washed samples, S1000-2W stands out owing to its higher FCC-Ni content, enabling rapid magnetic separation (approximately 90% in 5 s). Additional washing cycles do not further improve the sample performance.

Adsorption experiments with common pollutants such as hexavalent chromium and methylene blue show optimal removal efficiency at a low pH (=3), with rapid saturation achieved within 8–10 minutes. The adsorption kinetics closely follow a pseudo-first-order model, indicating that the process is dominated by physical adsorption. Isotherm analyses reveal that all samples follow the Langmuir, Freundlich, and Sips models. While S600-2W shows slightly better performance for Cr(VI) removal, likely due to its higher surface area and microporosity, S1000-2W exhibits superior adsorption capacity for methylene blue. This enhanced functionality is attributed to its more uniform and graphitic carbon structure, which besides preventing the oxidation of the Ni NPs, facilitates stronger π–π stacking interactions, ultimately leading to higher MB uptake despite the microporous advantage of S600-2W.

In conclusion, our findings highlight the synergistic interplay between Ni and carbon in these carbonized nanoparticles, which accelerates adsorption and enables efficient magnetic separation, thereby eliminating the need for costly and complex separation processes. It is also worth emphasizing that this tunability is particularly relevant for the design of magnetically recoverable adsorbents operating under acidic conditions. This work underscores the practical, scalable, and sustainable potential of Ni@C hybrid materials for advanced water remediation technologies targeting toxic dyes and heavy metals, paving the way for next-generation solutions to global water pollution challenges.

Author contributions

M. F. and A. C.-M. synthesized the samples. M. F. and P. A.-A. performed magnetic and XRD measurements, carried out most of the data analysis and prepared the original draft of the manuscript. A. A. collected TEM/HRTEM images and performed detailed analysis of the images. A. G.-C. and M. F. conducted the adsorption experiments and data analysis. P. G., M. R., J. A. B., J. I. P. & F. S.-G. were co-responsible for the conceptualization and methodology of the work. P. G., M. R., P. A.-A., J. I. P. & F. S.-G. were responsible for funding acquisition and supervision of the work. All authors participated in the writing, review and editing of the final version of the manuscript.

Conflicts of interest

There are no conflicts to declare.

Data availability

The data supporting this work have been included in the main article and in the supplementary information (SI). Supplementary information is available. See DOI: https://doi.org/10.1039/d6ta00283h.

Acknowledgements

This work was partially supported by the following research projects: (a) PIC2023-150968OA-100 and PID2022-138256NB-C21 (Spanish AEI, ERDF, EU); (b) SEK-25-GRU-GIC-24-113 and IDE/2024/000763 (SEKUENS, Principality of Asturias). A. A. acknowledges the Ramon y Cajal grant received from the Spanish Ministry of Science and Innovation (RYC2022-038426-

I). The authors also express their gratitude to the Scientific Service at the University of Oviedo, with special thanks to Dr D. Martinez-Blanco for his technical support.

Notes and references

1 A. Kumar, A. Nighojkar, P. Varma, N. J. Prakash, B. Kandasubramanian, K. Zimmermann and F. Dixit, *J. Hazard. Mater.*, 2023, **455**, 131568.
2 N. Morin-Crini, G. Crini, N. Fatin-Rouge, M. Fourmentin and G. Torri, *Environ. Chem. Lett.*, 2022, **20**, 2311.
3 B. Thomas, C. Vinka, L. Pawan and S. David, *Sci. Total Environ.*, 2022, **813**, 152345.
4 A. Ojha, D. Tiwary, R. Oraon, P. Singh and T. R. Cadaval, *Environ. Sci. Pollut. Res.*, 2021, **28**, 12345.
5 Q. Bu, B. Wang, J. Huang, S. Deng and G. Yu, *J. Hazard. Mater.*, 2013, **262**, 189.
6 X. Liu, Y. Zhang, Y. Liu, T. Zhang and J. Wang, *The Innovation*, 2021, **2**, 100076.
7 S. Dutta, B. Gupta, S. Srivastava and A. K. Gupta, *Mater. Adv.*, 2021, **2**, 4497.
8 P. Sharma, S. P. Singh, S. K. Parakh and Y. W. Tong, *Bioengineered*, 2022, **13**, 4923.
9 I. Khan, K. Saeed, I. Khan and N. Ali, *Water*, 2022, **14**, 242.
10 A. Ruhí, V. Acuña, D. Barceló and M. Petrovic, *Sci. Total Environ.*, 2016, **540**, 250.
11 J. Martín, J. G. del Río, I. Aparicio and E. Alonso, *Environ. Sci. Pollut. Res.*, 2018, **164**, 488.
12 P. Sharma, S. P. Singh, S. K. Parakh and Y. W. Tong, *Bioengineered*, 2022, **13**, 4923.
13 P. Patel, P. Gupta, K. Sujata and R. G. Solanki, *J. Cluster Sci.*, 2024, **35**, 191.
14 P. O. Oladoye, T. O. Ajiboye, E. O. Omotola and O. J. Oyewola, *Results Eng.*, 2022, **16**, 100678.
15 V. J. Sundar, J. Raghava Rao and C. Muralidharan, *J. Clean. Prod.*, 2002, **10**, 69.
16 S. B. Shen, R. D. Tyagi and J. F. Blais, *Environ. Tech.*, 2001, **22**, 1007.
17 B. Mella, A. C. Glanert and M. Gutterres, *Process Saf. Environ. Prot.*, 2015, **95**, 195.
18 K. Kapusta and K. Stańczyk, *Ecotoxicol. Environ. Saf.*, 2015, **112**, 105.
19 M. Pankiewicz-Sperka, K. Kapusta, W. Basa and K. Stolecka, *Energies*, 2021, **14**, 6533.
20 S. N. Che Nan, N. A. Mohd and Z. Zainal, *Mater. Sci. Forum*, 2022, **1076**, 109.
21 S. R. Dhokpande, S. M. Deshmukh, A. Khandekar and A. Sankhe, *Rev. Inorg. Chem.*, 2024, **64**, 78901.
22 M. Fadel, F. J. Martín-Jimeno, M. P. Fernández-García, F. Suárez-García, J. I. Paredes, J. H. Belo, J. P. Araújo, A. Adawy, D. Martínez-Blanco, P. Álvarez-Alonso, J. A. Blanco and P. Gorria, *J. Mater. Chem. C*, 2023, **11**, 4070.
23 M. Fadel, P. Álvarez-Alonso, M. Rivas, A. Adawy, J. L. Sánchez Llamazares, R. López-Antón, S. Q. Jan, R. Roy Chowdhury, D. A. Arena, H. Srikanth, J. A. Blanco, F. Suarez-García and P. Gorria, *Mater. Des.*, 2025, **259**, 114838.
24 F. J. Martín-Jimeno, F. Suárez-García, J. I. Paredes, A. Martínez-Alonso and J. M. D. Tascón, *J. Alloys Compd.*, 2021, **853**, 156789.
25 J. Rodríguez-Carvajal, *Physica B*, 1993, **192**, 55.
26 G. Sádovslá, P. Honcová, J. Morávková, I. Jirka, M. Vorokhta, R. Pilar, J. Rathousky, D. Kaucky, E. Mikysková and P. Sazama, *Carbon*, 2023, **206**, 211.
27 P. Song, D. Wen, Z. X. Guo and T. Koriakianitis, *Phys. Chem. Chem. Phys.*, 2008, **10**, 5057.
28 S. Zhang and C. Wang, *Methods Protoc.*, 2023, **6**, 123.
29 K. S. W. Sing, *Adv. Colloid Interface Sci.*, 1998, **76–77**, 3.
30 S. Dantas, K. C. Struckhoff, M. Thommes and A. V. Neimark, *Carbon*, 2021, **173**, 842.
31 W. Braun, H.-P. Steinrück and G. Held, *Surf. Sci.*, 2005, **575**, 343.
32 D. Yan, L. Zhang, Z. Chen, W. Xiao and X. Yang, *Acta Phys. Chim. Sin.*, 2021, **37**, 567.
33 D. Martínez-Blanco, P. Gorria, J. A. Blanco, M. J. Pérez and J. Campo, *J. Phys.: Condens. Matter*, 2008, **20**, 335213.
34 M. P. Fernández-García, P. Gorria, M. Sevilla, J. A. Blanco and A. B. Fuertes, *J. Phys. Chem. C*, 2011, **115**, 5294.
35 P. Gorria, M. P. Fernández-García, M. Sevilla, J. A. Blanco and A. B. Fuertes, *Phys. Status Solidi RRL*, 2009, **3**, 4.
36 N. Rinaldi-Montes, P. Gorria, D. Martínez-Blanco, Z. Amghouz, A. B. Fuertes, L. Fernández Barquín, J. Rodríguez Fernández, L. Olivi, G. Aquilanti and J. A. Blanco, *Nanoscale*, 2014, **6**, 457.
37 J. M. D. Coey, *Magnetism and Magnetic Materials*, Cambridge University Press, 2010.
38 A. Bouremana, A. Guittoum, M. Hemmous, D. Martinez-Blanco, P. Gorria, J. A. Blanco and N. Benrekaa, *Mater. Chem. Phys.*, 2015, **160**, 435.
39 Y. T. Jeon, J. Y. Moon, G. H. Lee, J. Park and Y. Chang, *J. Phys. Chem. B*, 2006, **110**, 1187.
40 E. G. C. Neiva, M. M. Oliveira, L. H. Marcolino and A. J. G. Zarbin, *J. Colloid Interface Sci.*, 2016, **468**, 34.
41 R. Shokrani Havigh and H. Mahmoudi Chenari, *Sci. Rep.*, 2022, **12**, 345.
42 J. Wang and X. Guo, *Chemosphere*, 2022, **309**, 136789.
43 J. A. Greathouse, K. L. Johnson, S. E. Feller and P. R. Kent, *Clays Clay Miner.*, 2015, **63**, 185.
44 E. Santoso, S. Edi, Y. Kusumawati and H. Bahruji, *Mater. Today Chem.*, 2020, **16**, 100233.
45 X. Liu, Y. Zhang, Y. Liu and T. Zhang, *Int. J. Biol. Macromol.*, 2022, **222**, 2615.
46 K. Z. Elwakeel, A. M. Elgarahy, Z. A. Khan, M. S. Almughamisi and A. S. Al-Bogami, *Mater. Adv.*, 2020, **1**, 1546.
47 M. Rajabi, K. Mahanpoor, O. Moradi and A. J. Moradi, *J. Nanostruct. Chem.*, 2023, **13**, 43.
48 B. Royer, N. F. Cardoso, E. C. Lima and J. C. Vaghetti, *J. Hazard. Mater.*, 2009, **164**, 1213.
49 A. F. Hassan, A. M. Abdel-Mohsen and M. M. G. Fouda, *Carbohydr. Polym.*, 2014, **102**, 192.
50 E. Altıntıg, H. Altundag, M. Tuzen and A. Sarı, *Chem. Eng. Res. Des.*, 2017, **122**, 151.

51 A. Allafchian and A. R. Gharaati, *Int. J. Biol. Macromol.*, 2023, **242**, 123456.
52 K. Saini, R. Sharma, V. Gupta and A. Singh, *Environ. Sci. Pollut. Res.*, 2023, **231**, 116165.
53 M. Jain, V. K. Garg, K. Kadirvelu and M. Sillanpää, *Water Resour. Ind.*, 2018, **20**, 54.
54 Y. Xiao, H. Liang and Z. Wang, *Mater. Res. Bull.*, 2013, **48**, 3910.
55 T. V. Tuyen, H. T. Tran, T. H. Nguyen and T. T. Le, *Appl. Phys. A*, 2020, **126**, 1.